Interplay between Anakonda, Gliotactin, and M6 for Tricellular Junction Assembly and Anchoring of Septate Junctions in Drosophila Epithelium

Thomas Esmangart de Bournonville, Roland Le Borgne

Graphical abstract

Click here to access/download;Graphical Abstract;Esmangart de Bournonville_Graphical Abstract_290720.jpg

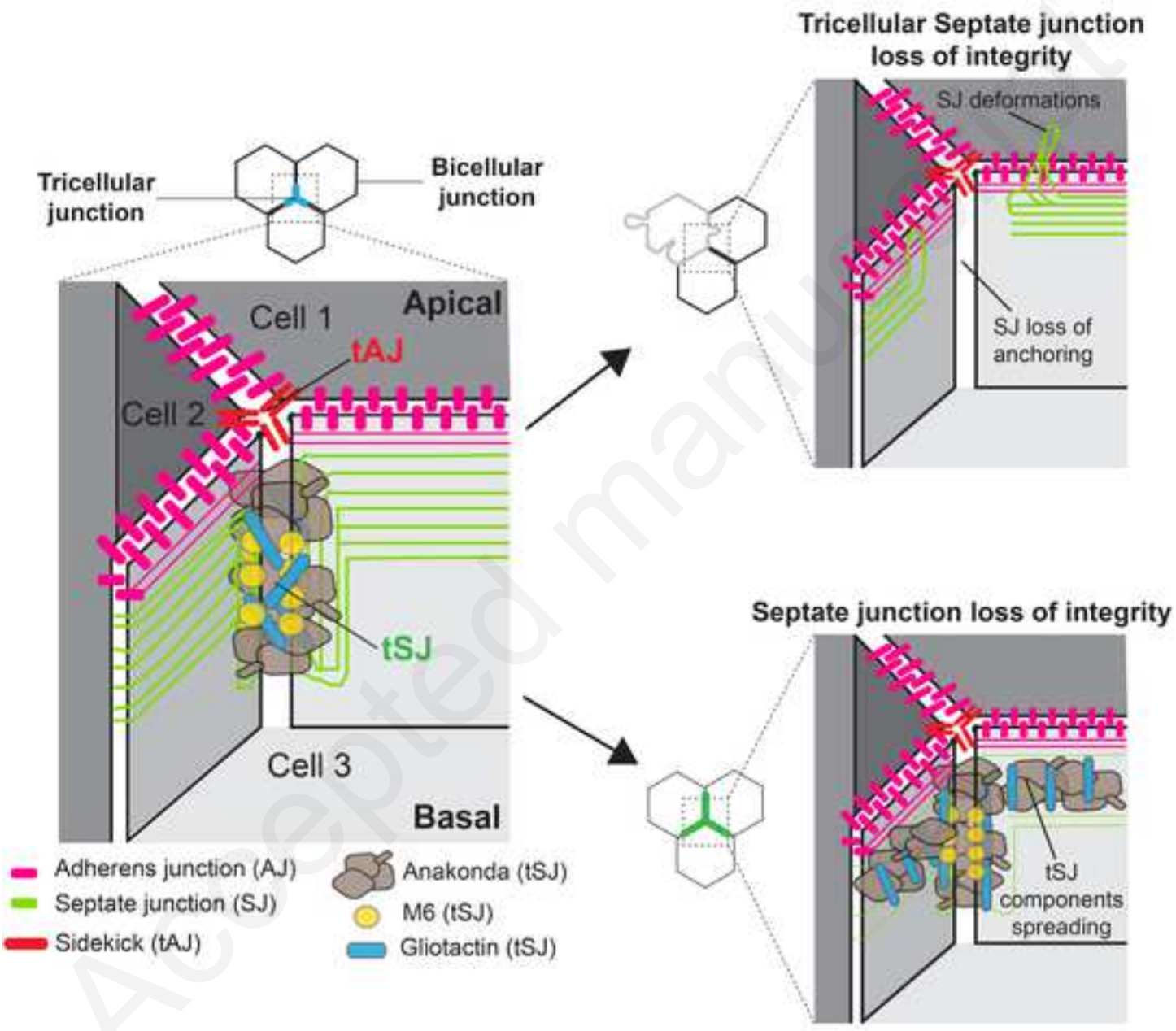

Interplay between Anakonda, Gliotactin and M6 for tricellular junction assembly and anchoring of septate junctions in *Drosophila* epithelium

Thomas Esmangart de Bournonville[1,2] and Roland Le Borgne[1,2,3]

[1]Univ Rennes, CNRS, IGDR (Institut de Génétique et Développement de Rennes) - UMR 6290, F- 2 av du Pr Bernard, 35000 Rennes, France

[2]Equipe Labellisée Ligue Nationale contre le cancer

[3] Lead Contact

Correspondence: roland.leborgne@univ-rennes1.fr

phone: +33 223 234 894

Orcid: http://orcid.org/0000-0001-6892-278X

Summary

In epithelia, Tricellular junctions (TCJs) serve as pivotal sites for barrier function and integration of both biochemical and mechanical signals [1-3]. In *Drosophila*, TCJs are composed of the transmembrane proteins Sidekick, at the Adherens Junction level (AJ), which plays a role in cell-cell contact rearrangement [4-6]. At the Septate Junction level (SJ), TCJs are formed by Gliotactin (Gli) [7], Anakonda (Aka) [8, 9] and the Myelin proteolipid protein (PLP) M6 [10, 11]. Despite previous data on TCJ organization [12-14], TCJ assembly, composition and links to adjacent bicellular junctions (BCJs) remain poorly understood. Here, we have characterized the making of TCJs within the plane of adherens junctions (tAJ) and the plane of septate junctions (tSJ) and report that their assembly is independent of each other. Aka and M6, whose localizations are interdependent, act upstream to localize Gli. In turn, Gli stabilizes Aka at tSJ. Moreover, tSJ components are not only essential at vertex as we found that loss of tSJ integrity induces micron-length bicellular SJs deformations. This phenotype is associated with the disappearance of SJ components at tricellular contacts, indicating that bSJs are no longer connected to tSJs. Reciprocally, SJ components are required to restrict the localization of Aka and Gli at vertex. We propose that tSJs function as pillars to anchor bSJs to ensure the maintenance of tissue integrity in *Drosophila* proliferative epithelia.

Results

TCJ *de novo* assembly and SJ regulation during cytokinesis

The notum of the *Drosophila melanogaster* is a proliferative monolayer epithelium, allowing the study of cell division in time and space. Epithelial cytokinesis is a multicellular process during which a new BCJ interface and two new TCJs are established (Figures 1A and 1C). To decipher the *de novo* assembly of TCJ (tAJ and tSJ) that takes place in cytokinesis, we imaged the AJ and the midbody using the non-muscle Myosin II light chain tagged with red fluorescent protein (Spaghetti Squash, Sqh::RFP; [15]) together with the tAJ marker Sdk::GFP [16] or the tSJ markers GFP::M6 [17] and Aka::GFP [8]. All fluorescent markers are inserted at the locus, giving rise to functional reporters expressed at physiological level. In telophase,

following actomyosin ring constriction, Sqh is recruited at the new cell-cell interface and in neighboring cells at AJ level as reported ([18-20], Figure 1A). In all cases, the transition from metaphase to anaphase, defined by the frame just before the onset of cell elongation, was considered to be t0 (time is indicated in min:sec). Initiation of the formation of new adhesive contacts between daughter cells occurs at t10 (Figure 1B; Movie S1) [18, 19, 21]. Concomitantly, the first signal of Sdk::GFP appears at the new vertex around t10-t13 (Figures 1B and 1F; Movie S1). Basal to AJ, as previously described [15, 22], the contractile ring remains anchored to the plasma membrane at the SJ level, connecting the divided cells to their neighbours and resulting in the formation of finger-like protrusions (FLP) upon midbody formation (Figures 1C and S1A-B'; Movie S2). The tSJ markers GFP::M6 (Movie S3) and Aka::GFP first appear in the form of puncta adjacent to the midbody at t15 and t17 respectively (Figures 1D and 1E) [15]. Their signals then spread laterally until they form a continuous tSJ strand (t50, Figures 1D-F; Movie S3). Thus, assembly of the tAJ and tSJ are spatially and temporally independent (Figure 1G).

The presence of tSJ components along the FLP connected to the midbody during cytokinesis raises the question of the role of tSJ in FLP maintenance. In wild-type conditions, FLPs labeled with the core SJ component ATP-α::GFP [15], formed 1µm below AJ at t5 as the result of actomyosin cytokinetic ring constriction (Figures 1SA-S1B) and displayed a characteristic "U" shape between t5 and t10 (Figures S1A'-S1B'; Movie S1). Midbody was centered in 71% of the cases resulting in the formation of two FLPs of similar length (Figures S1A', S1B and S1E). Upon loss of Aka using the *aka*^{L200} null mutant [8], the midbody is off-centered leading to two FLPs of unequal length (62% of cases compare to only 29% for wild-type cells; Figures S1C-S1E; Movie S4). In addition, we observed that ATP-α::GFP signal is inhomogeneous in those FLPs compared to wild-type conditions (Figures S1C'-S1D; Movie S4). These results indicate that Aka ensures the symmetry in FLP formation as well as the SJ components distribution, suggesting a role for Aka in regulating bicellular septate junction (bSJ) (Figure S1F; see below).

The fact that the recruitment of Sdk and Aka/M6 are spatially and temporally independent during cytokinesis (Figure 1) suggests that tSJ and tAJ assembling and perhaps functioning are independent.

Interplay between tAJ and tSJ components

In order to analyze of the relationship between tAJ and tSJ, we next analyzed the consequence of loss of Sdk on tSJ. We used the homozygous viable null allele *sdk*$^{\Delta 15}$ [23] and observed no differences of Aka signals (Figures S2A-S2B'). Conversely, we studied the loss of tSJ integrity using the *aka*^{L200} mutant on Sdk localization. No differences in the localization of Sdk were observed between wild-type and *aka*^{L200} cells (Figures S2C and S2C'). These data indicate that the localization, recruitment and/or stabilization of Sdk and Aka at TCJ are independent one of each other.

Then, we investigated the relationship between the three tSJ components. Loss of Aka leads to Gli (Figures S2D and S2D') and GFP::M6 (Figures 2A and 2A') disappearance from tSJ. This is true even when only one cell contributing to the vertex is mutant for Aka, thereby confirming that Aka is an upstream regulator in the notum, as described in *Drosophila* embryo [8]. We next studied the role of M6 on Aka and Gli localization and found that loss of M6, using *M6*^{w186} null mutant [11], leads to Aka (Figures 2B and 2B') and Gli (Figures S2E and S2E') no longer accumulating at vertex. Therefore, M6 and Aka are both upstream regulators of tSJ assembly. However, and unlike Aka, loss of M6 from one cell contributing to the vertex triggers the reduction in Aka signal (Figures 2B-2B'') rather than a complete disappearance. Gli signal is still detectable in that case too (Figure S2E).

Because Gli activity is dispensable for Aka localization at tSJ in *Drosophila* embryo [8], we tested if this was also the case in the pupal notum. Unexpectedly, we found a decrease in the intensity of Aka signal in *Gli*^{dv3} mutant cells (Figures 2C and 2C'). We next tested the possibility that the stabilization of Aka at tSJ is modified upon loss of Gli using FRAP. Our experiments revealed that upon loss of Gli, immobile fraction of Aka::GFP drastically dropped to 0.30 compared to 0.75 in wild-type conditions, 20 minutes after photobleaching (Figures S2F and S2G) with a mild reduction of the rate of fluorescence recovery ($t_{1/2}$ = 318s in *Gli*^{dv3} and $t_{1/2}$ = 361s in Wild type).

Therefore, while being dispensable to localize Aka at tSJ, Gli influences the time of residency of Aka, revealing an interplay between Aka, Gli and M6 (Figure 2D).

Loss of tSJ disrupts SJ integrity at both bSJ and vertices and induces SJ deformations

In addition to defects in tSJ assembly, our time-lapse analyses also revealed defects in the integrity of bSJ in interphase upon loss of Aka. Indeed, it caused the appearance of 1 to 3 micron-long membrane deformations labelled using GAP43::mCherry (Figures

S3A and S3B). These membrane deformations are located within the plane of SJ, positive for the SJ core components including Cora (Figure 3A), ATP-α::GFP (Figure 3B) and Nrx-IV (Figure 3C), as well as Dlg (Figure 3D). This phenotype was not only observed using several *aka* mutant alleles (data not shown), upon silencing of Aka (Figure S3A and S3B) but also upon loss of Gli (Figure S3C) indicating that loss of Aka or its stability at tSJ is associated with SJ membrane deformations. Using Nrx-IV, we observed that many deformations are found apical, close to and/or within the plane of DE-cad albeit not colocalizing with it (Figures 3E-3H'). We also observed Nrx-IV signal disappearance or drastic decrease from vertices in aka^{L200} cells (Figures 3I and 3I'). While similar results were observed for ATP-α::GFP (data not shown), in contrast Dlg (Figures 3I and 3I') and GAP43::mCherry (Figures S3A and S3B) remained present at the vertex. This data argues for a depletion of SJ core components from the vertex. The loss of Gli induced similar results on Nrx-IV presence at vertex (data not shown). These results raise the question of how and why loss of tSJ integrity causes SJ deformations (Figure 3D') and prevents the presence of SJ core components at the vertex (Figure 3J).

Since SJ-containing membrane deformations localize in part at AJ level and that AJs are the sites of actomyosin driven mechanical forces of the tissue [24, 25], we probed if forces were involved in the stabilization of these deformations. Using two-photon laser-based nano ablation, we cut the tips of deformations to reveal possible pulling or pushing forces (Figure S3D). No significant recoil or changes in the shape of deformations were observed upon ablation. Then, we probed lateral forces by cutting the bSJ close to the deformation and again, we revealed no deformation shape changes after ablation (Figure S3E). In accordance with those results, nor Sqh or Actin marked by phalloidin were enriched in those deformations, excluding the possibility that AJ components (DE-cad; Figures 3E-3H') or actomyosin (Figures S3F and S3G) stabilized them. Next, we tested if changes in SJ components dynamics could be responsible for the induction of those deformations, by FRAP approach on ATP-α::GFP (Figures S3H-J). Wild-type cells exhibited slow turnover at bSJ ($t_{1/2}$ = 280s) with an immobile fraction of 0.67 at 18 min after photobleaching (Figures S3H and S3K). In aka^{L200} cells, the kinetics of recovery were similar to wild-type condition ($t_{1/2}$ = 294s) but exhibited a slight increase of the immobile fraction of 0.76 at 18 min after photobleaching (Figures S3I and S3K). Moreover, SJ containing membrane deformations revealed a higher immobile fraction of 0.82 at 18 min after

photobleaching, while the $t_{1/2}$ = 296s remained similar (Figures S3J and S3L). Therefore, loss of tSJ led to an increased residency time of ATP-α::GFP. This might explain why the steady state levels of ATPα::GFP signal is higher in membrane deformations (Figures 3B, 3C, 3G and S3D-F).

bSJs restrict the localization of tSJ components at vertices

Loss of tSJ leads to detachment of bSJ from vertex and changes in the dynamics of recovery of SJ core components in membrane deformations, suggesting a possible physical connection between tSJ and bSJ. This prompted us to study the consequence of loss of function of bSJ on the localization of tSJ proteins. We found that depletion of the SJ core component Cora leads to the spreading of Aka along bSJ (Figures 4A-4C'). The lateral spreading of Aka was not due to an increase in the length of bicellular junction adjacent to the vertex (Figures 4D-4E). Similar results were obtained upon depletion of Nrx-IV (Figures S4A-S4C'). Finally, the spreading of Gli was equally observed in Nrx-IV RNAi context (Figures S4D-S4F') and Cora RNAi (data not shown). Together, our results demonstrate that bSJ integrity is required to confine tSJ components localization at the vertex.

Discussion

Here, we provided evidence that the recruitment, localization and stabilization of tAJ and tSJ are spatially and temporally independent. Among tSJ, Aka and M6 were found to be upstream regulators of tSJ while Gli stabilized Aka at tSJs. Moreover, we uncovered that tSJ components are essential to maintain SJ homeostasis both in interphase and during mitosis. Conversely, SJ integrity is required for tSJ components to be confined at vertices. Based on these results, we propose a model of mutual dependence in which tSJs act as pillars to anchor SJ strands at vertices while SJ core components act to restrict tSJ components at the vertices (Figures 4F-4H).

Our study of TCJ assembly showed that like AJ and SJ, tAJ is established first, prior to tSJ. *De novo* formation of AJ occurs concomitantly to Sdk recruitment at vertices (this study; [18, 19, 21]), suggesting a coupled mechanism to ensure AJ mechanical integrity at both bicellular and tricellular junctions. Once tAJs are formed, tSJ components begin to be recruited at FLP level, with GFP::M6 detected before Aka::GFP. It is interesting to note that, during cytokinesis in vertebrates, Tricellulin and Lipolysis-stimulated lipoprotein receptor LSR, the main components of tight Tricellular

junction (tTJ) [26-28], are also recruited with different timing [29]. Although we cannot exclude that the difference in stoichiometry at tSJ could account for the delay in Aka::GFP appearance compared to GFP::M6, these results suggest similarities for tSJ and tTJ assembly.

Here we show that Aka and M6 are interdependent for their localization at tSJ, and are acting upstream of Gli in the tSJ assembly pathway. Nonetheless, our analyses of clone borders suggest some differences in the requirement of Aka and M6 in tSJ assembly. Structure function analyses and mode of subcellular localization of M6, a small four-pass transmembrane proteolipid protein will help understanding its activity, stoichiometry, and relationship with Aka. In addition, it will be interesting to determine whether the mammalian ortholog of M6, enriched in CNS [30, 31] also localizes at TCJ and exerts similar function in vertebrates. Our study also revealed that Gli is required for the maintenance of Aka localization at tSJ. Thus, Gli is not simply a downstream effector of Aka and M6, indicating an interplay between Aka, M6 and Gli in regulating tSJ assembly, stability and function. Loss of LSR in vertebrates leads to the spreading of Tricellulin, resembling the loss of Aka on Gli [27]. Whether or not Tricellulin plays a role on LSR stability remains to be determined.

Transmission electron microscopy (TEM) revealed that vertices in invertebrates are intercellular space spanned vertically with diaphragms [12-14]. SJs were also characterized by TEM as belt-like strands of septa [12-14, 32]. Moreover, SJ proteins partially colocalize with tSJ proteins (this study; [33]), suggesting that SJs and tSJs are physically connected. Our results are compatible with a model in which Gli interacts directly with SJ components proteins. Another hypothesis could state that the loss of Aka stability by loss of Gli triggers SJ core components exclusion from the vertex. If so, the effect of loss of Gli on Aka stability might be indirectly mediated since they are not reported to co-immunoprecipitate [8]. Gli is part of Neuroligin family [34], a set of proteins involved in synapse formations [35] and synaptic transmission [36, 37]. Moreover, recent studies highlighted physical interaction between MGDA proteins and Neuroligin [38-40]. MGDA proteins are composed of six N-terminal Ig domains and one fibronectin type III domain [41], which looks like Neuroglian (Nrg) organization, a SJ core component protein, displaying also six N-terminal Ig domains followed by five fibronectin type III domain [42]. MGDA are reported interacting with Neuroligin via their first two Ig domains [38-40]. Knowing that Nrg formed a complex with Cora, ATP-α and

Nrx-IV [43, 44], the link between tSJ and SJ could be Gli binding Nrg, making tSJ the pillar required to anchor SJ strands.

Epithelial cells lacking CrebA showed excess of membrane and SJ components [45]. Also, another recent study [46] highlighted that subperineurial glial cells lacking SJ integrity compensate by overexpressing SJ components and making more cellular membrane. It is conceivable that the loss of SJ anchorage at tSJs could result in a permeability defect that is detected at the cell level. In an attempt to compensate for the lack of permeability, more SJ proteins and membrane components would be targeted to the plasma membrane. Such excessive amount of SJ proteins combined with their slow turnover would cause the local enrichment resulting in BCJ elongation and thus in membrane deformations. However, how cells could sense SJ permeability defects and the molecular processes leading to SJ deformations remains elusive at present.

The mutual exclusion of bSJ and tSJ components combined with the pillar model proposed above raise the question about origins of tSJ proteins localization. Inducing loss of SJ integrity leads to Aka and Gli spreading along BCJ as shown here upon Cora or Nrx-IV depletion. The space freed up by the loss of SJ may allow tSJ components to move to this location [47]. Another explanation could be that tSJ components roles are multiple. One is to anchor SJ strands at vertices to ensure their shape and integrity. Another one could be that they also play a role in permeability function, by localizing SJ components in close vicinity of the vertex or by playing a filter role themselves. Therefore, their spreading at BCJ upon SJ loss of integrity could be a compensatory mechanism.

Since permeability barrier function is essential for the maintenance of epithelial integrity in both invertebrates and vertebrates, it will be interesting to determine if these relationships between TCJs and BCJs are conserved.

Acknowledgements

We thank Dr. Luschnig, Klämbt, Martin, Treisman, Uv, Xu, the Bloomington *Drosophila* Stock Center, the Vienna Drosophila Resource Center, InDroso and the Developmental Studies Hybridoma Bank for providing fly stocks and antibodies. We also thank the Microscopy Rennes Imaging facility. We thank S.Luschnig, M. Hollmann and members of R.L.B.'s laboratory for critical reading of the manuscript. This work

was supported in part by the ARED program from the Région Bretagne, La Ligue contre le Cancer-Equipe Labellisée and Agence Nationale de la Recherche CytoSIGN (ANR-16-CE13-004-01) to R.L.B.

Author Contributions

Conceptualization, Methodology, Investigation, Formal Analysis, Visualization, Writing – Original Draft, – Review & Editing, T.E.d.B and R.L.B.; Funding Acquisition, R.L.B.; Supervision, R.L.B.

Declaration of Interests

The authors declare no competing interests

Figure Legends

Figure 1: TCJ assembly during epithelial cytokinesis

(A and C) Schematic of tAJ (A) and tSJ (C) assembly during cytokinesis. In this and the following panels, M, D and N represent mother, daughter and neighboring cells respectively. Magenta signal represents Sqh::RFP enrichment at the new interface and in neighboring cells (A) or the midbody between the FLP forming at SJ level (C). Red dots show tAJ (A) and green lines show tSJ (C). (B, D and E') Time-lapse imaging of Sqh::RFP (magenta), Sdk::GFP (B'), GFP::M6 (D') and Aka::GFP (E') in dividing cells. The dashed line highlights the divided cell and the two new cells. Yellow arrowheads show the first appearance of GFP signal. White arrowheads show the two new TCJs formed at AJ level. White squares show high magnifications of Sdk::GFP (B') arrival at new vertex or GFP::M6 (D') /Aka::GFP (E') first appearance close to the midbody (magenta). (F) Plot of the mean times of the first appearance after anaphase onset of Sdk::GFP (purple dots, n = 26 divisions, 4 pupae), GFP::M6 (green squares, n = 64 divisions, > 5 pupae) and Aka::GFP (dark green triangles, n = 36 divisions, > 5 pupae). Bars show Mean ± SD, **** $p < 0.0001$, unpaired t test. (G) Schematic of tAJs and tSJs assembly 20 minutes after anaphase onset. Magenta signal represents the midbody between the FLP forming at SJ level. Dark blue dots show new tAJs characterized by Sdk::GFP and dark green lines show the formation of new tSJs characterized by GFP::M6 and Aka::GFP, below tAJs. In these and all other panels time is min:sec (B, D and E) with t0 corresponding to the anaphase onset, and scale bars are 5µm. Distances correspond to the position relative to the plane of AJ labeled with Sqh::RFP. **See also Figure S1.**

Figure 2: Aka and M6 are upstream regulators of tSJ

(A-C) nota stained for DE-cad (anti-DE-cad, green) after heat-shock to induce clone of wild type (A and C nls::RFP positive; B, GFP negative) and mutant cells (A and C nls::RFP negative; B, GFP positive) for tSJ components. (A) Localization of M6 (GFP::M6 + anti-GFP, magenta). Wild-type and aka^{L200} cells are separated by the dashed yellow line. M6 is enriched at the TCJ at wild-type vertex (blue square) and is no longer detected at vertex upon loss of Aka from one cell adjacent to the vertex (pink square) or at a vertex of three aka^{L200} cells (orange square). (B) Localization of Aka (anti-Aka, magenta). Wild type and $M6^{w186}$ mutant cells are separated by the dashed yellow line. Aka is enriched at the TCJ at wild-type vertex (blue square) and upon loss

of M6 from one cell adjacent to the vertex (pink square) but the accumulation disappears at vertex of three *M6^{w186}* mutant cells (orange square). (A' and B') Histograms representing the percentage of presence (black) or absence (gray) of M6 and Aka accumulation at the vertex between 3 wild type cells, 2 wild type and 1 *aka^{L200}* cell (A') or 1 *M6^{w186}* cell (B') or 3 *aka^{L200}* cells (A') or 3 *M6 ^{w186}* cells (B') (n = 100 vertices, > 5 pupae for each experiment). (B'') Plot of the standardized Aka signal at a wild-type vertex (orange squares) and a vertex of two wild-type / one *M6^{w186}* cells (green circles). (n = 39 and 35 vertices respectively, 3 pupae). Bars show Mean ± SD, **** $p < 0.0001$, unpaired t test. (C) Localization of Aka (anti-Aka, magenta). Wild type and *Gli^{dv3}* cells are separated by the dashed yellow line. Orange and blue squares show Aka signal in *Gli* and Wild type conditions respectively. (C') Plot of the standardized Aka signal at vertex in wild type (orange squares) and *Gli^{dv3}* cells (blue circles). (n = 100 vertices each, > 5 pupae). Bars show Mean ± SD, **** $p < 0.0001$, unpaired t test. (D) Schematic of the interplay of TCJ components. The scale bars represent 5µm. All images are maximum projection. **See also Figure S2.**

Figure 3: tSJs regulate the shape of SJ and ensure the anchoring of SJ core components at the vertex

(A-D) SJ morphology visualized with Cora (anti-Cora), ATP-α (ATP::GFP), and Nrx-IV (anti-Nrx-IV) or other SJ component Dlg (anti-Dlg) in wild type and *aka^{L200}* cells, separated with the dashed yellow line. Yellow arrowheads indicate micrometric size deformations of SJ. (D') schematic of the bSJ membrane deformations observed upon loss of Aka. (E-H') Localization of Nrx-IV (anti-Nrx-IV, magenta) in notum marked by DE-cad (anti-DE-cad, green). (E-E''' and G-G''') show different planar sections separated by 0.5µm in wild type and *aka^{L200}* cells. (F and H) show maximum projection of the transversal section depicted by the yellow rectangles. (F' and H') Plots representing DE-cad (green line) and Nrx-IV (magenta line) signals as a function of cell transversal length represented in transverse sections. Black dashed lines show the presumptive boundary between AJ and SJ. (I) Localization of Dlg (anti-Dlg, green) and Nrx-IV (anti-Nrx-IV, magenta) in *aka^{L200}* cells after maximal projection. White squares show high magnification of a vertex in *aka^{L200}* cells. Yellow dashed rectangle shows the line scan used between two vertices represented by 1 and 2 to obtain (I') Plot representing Dlg (green line) and Nrx-IV (magenta line) signals as a function of the length of cell-cell boundary.

(J) Scheme showing the loss of *aka*^{L200} effect on SJ core component. Magenta lines show SJ core component, green lines the tSJ and black lines the membrane as well as Dlg protein. The scale bars represent 5µm or 1µm in (F and H). **See also Figure S3.**

Figure 4: SJ integrity is required to confine tSJ components at vertex

(A) Localization of Aka (anti-Aka, magenta) in cells marked by Cora (anti-Cora, green) in wild type and cells expressing UAS::Cora-RNAi under *pnr*-Gal4 control. The dashed yellow line separates wild type and Cora-RNAi cells. Aka spreads at the BCJ upon knock-down of Cora. White squares show (B and C) magnification of wild type and knock-down cells for Cora. Yellow lines show the line scan used to obtain (B' and C') plots representing Cora (green line) and Nrx-IV (magenta line) signals as a function of the length of cell-cell boundary in wild type and Cora-RNAi cells respectively. (D) Plot of the diameters (µm) of circles including maximal Aka signal at vertex in wild type (orange squares) and Cora-RNAi cells (blue circles) (n= 50 vertices, > 5 pupae). (E) Plot of the length (µm) of BCJ adjacent of wild type vertices (orange squares) and Cora-RNAi vertices (blue circles) (n= 50 BCJ, > 5 pupae). Bar show Mean ± SD, **** $p < 0.0001$, ns: non-significant, unpaired t test. (F) Schematic of the TCJ general organization in *Drosophila* notum. (G) Upon loss of tSJ integrity, SJ strands are no longer anchored on tSJ complex, leading to loss of SJ components presence at vertex and SJ deformations inductions in both AJ and SJ level. (H) Upon silencing of SJ core components, Aka and Gli spread at BCJ and are no longer restricted at the vertex. The scale bars represent 5µm. **See also Figure S4.**

STAR Methods

RESOURCE AVAILABILITY

Contact for Reagent and Resource Sharing

Further information and requests for resources and reagents should be directed to and will be fulfilled by the Lead Contact, Roland Le Borgne (roland.leborgne@univ-rennes1.fr)

Materials Availability

This study did not generate new unique reagents.

Data and Code Availability

This study did not generate/analyze [datasets/code].

EXPERIMENTAL MODEL AND SUBJECT DETAILS

Experimental model

Drosophila strains

Drosophila melanogaster stocks were maintained and crossed at 25°C. The following strains were obtained as follow : Aka::GFP, *Gli*^{dv3}, FRT40A / CyO was obtained by recombining Aka::GFP [8] with *Gli*^{dv3}, FRT40A / CyO [7]; *hs*-FLP ; *aka*^{L200}, FRT40A / CyO was obtained by crossing *aka*^{L200}, FRT40A / CyO [8] with *hs*-FLP ; If / CyO and appropriate flies were selected; *hs*-FLP ; If / CyO ; *M6*^{w186}, FRT79E / TM6, *Tb*^{1} was obtained by crossing w* ; UAS-Ras^{V12} ; *M6*^{w186}, FRT79E / TM6, *Tb*^{1} [11] with *hs*-FLP ; If / CyO ; MKRS / TM6, *Tb*^{1} and appropriate flies were selected ; *ubi*-RFP nls, FRT40A / (CyO) ; ATP-α::GFP, *sqh*-Sqh::mCherry/(TM6, *Tb*^{1}) was constructed by crossing ATP-α::GFP, *sqh*-Sqh::mCherry / (TM6, *Tb*^{1}) [15] with *ubi*-RFP nls, FRT40A / (CyO) ; MKRS / TM6, *Tb*^{1} and appropriate flies were selected. Somatic clones were induced using the FLP-FRT technique using the hs-FLP and by two heat shocks (60 min at 37°C) at second and third instar larvae.

Genotypes

Figure 1

(B) Sqh::RFP^{crispr} / Sdk::GFP obtained by crossing Sqh::RFP^{crispr} with Sdk::GFP

(D) Sqh::RFP^{crispr} ; ; GFP::M6 obtained by crossing Sqh::RFP^{crispr} with GFP::M6

(E) Sqh::RFP^{crispr} ; Aka::GFP obtained by crossing Sqh::RFP^{crispr} with Aka::GFP

Figure 2

(A) *hs*-FLP ; *aka*^{L200}, FRT40A / *ubi*-RFP nls, FRT40A obtained by crossing *aka*^{L200}, FRT40A / CyO with yw, *hs*-FLP ; *ubi* -RFP nls, FRT40A / (CyO)

(B) *hs*-FLP ; Act>y+Gal4, UAS-GFP ; *M6*^{w186}, FRT79E / *tub* -Gal80, FRT79E obtained by crossing yw, *ey*-FLP ; Act>y+Gal4, UAS-GFP ; *tub*-Gal80, FRT79E with *hs*-FLP ; If/CyO ; *M6*^{w186}, FRT79E / TM6, *Tb*^{1}

(C) *hs*-FLP ; *Gli*^{dv3}, FRT40A/ *ubi*-RFP nls, FRT40A obtained by crossing *Gli*^{dv3}, FRT40A/CyO with yw, *hs*-FLP ; *ubi*-RFP nls, FRT40A / (CyO)

Figure 3

(A, C, D, E, G and I) *hs*-FLP; *aka*^{L200}, FRT40A / *ubi* -RFP nls, FRT40A obtained by crossing *aka*^{L200}, FRT40A / CyO with yw, *hs*-FLP ; *ubi* -RFP nls, FRT40A / (CyO)

(B) *hs*-FLP ; *aka*^{L200}, FRT40A / *ubi*-RFP nls, FRT40A ; ATP-α::GFP, sqh-Sqh::mCherry/ + obtained by crossing ; *ubi*-RFP nls, FRT40A/(CyO) ; ATP-α::GFP, *sqh*-Sqh::mCherry / (TM6, *Tb*^{1}) with *hs*-FLP ; *aka*^{L200}, FRT40A / CyO

Figure 4

(A-C) UAS-Cora-RNAi / *pnr*-Gal4 obtained by crossing UAS-Cora-RNAi with *pnr*-Gal4 / TM6, *Tb*^{1}

METHOD DETAILS

Immunostaining

Pupae were collected at puparium formation (0 hours After Puparium Formation, 0h APF) and were dissected at 16h30 APF using Cannas microscissors (Biotek, France) in 1X Phosphate-Buffered Saline (1X PBS, pH 7.4) and fixed 15 min in 4% paraformaldehyde at room temperature [55]. Following fixation, dissected nota were permeabilized using 0.1% Triton X-100 in 1X PBS (PBT), incubated with primary antibodies diluted in PBT for 2 hours at room temperature. The following primary antibodies were used: Cora (mouse, 1:200, DSHB, C615.16), DE-Cad (rat, 1:500, DSHB, DCAD2), Dlg (mouse, 1:500, DSHB, 4F3), GFP (mouse, 1:200, Roche, clone 7.1), Aka (rabbit, 1:2000, a gift from A. Uv) [8], Gli (mouse, 1:200, a gift from V. Auld) [48], Sdk (guinea pig, 1:200, a gift from J. Treisman) [23], Nrx-IV (rabbit, 1:1000, a gift from C. Klämbt) [49].

After 3 washes of 5 minutes in PBT, nota were incubated with secondary antibodies (Jackson ImmunoResearch Laboratories) diluted at 1:1000 in PBT for 1 hour, followed by 2 washes in PBT, and one wash in PBS, prior mounting in 0,5% N-propylgallate dissolved in 90% glycerol/PBS 1X final.

Live-imaging and image analyses

Live imaging was performed on pupae aged for 16h30 APF at 25°C. Pupae were adhered on a glass slide with a double-sided tape, and the brown pupal case was

removed over the head and dorsal thorax using microdissecting forceps. Pillars made of 4 and 5 glass coverslips were positioned at the anterior and posterior side of the pupae, respectively. A glass coverslip covered with a thin film of Voltalef 10S oil is then placed on top of the pillars such that a meniscus is formed between the dorsal thorax of the pupae and the glass coverslip [56]. Images were acquired with a LSM Leica SPE, SP5 or SP8 equipped with a 63X N.A. 1.4. and controlled by LAS AF software. Confocal sections (z) were taken every 0.5 µm. For figures representation, images were processed with Gaussian Blur σ = 1.1. All images were processed and assembled using Fiji software [53] and Adobe Illustrator.

Fluorescence recovery after photobleaching

FRAP experiments were performed in pupae expressing Aka::GFP with RFP-nls used as a marker of *Gli*^{dv3} cells. Aka::GFP was bleached (488 nm laser at 60% power, 2 iterations of 1.293 s, square ROI of 2µm*1.5µm) using a LSM Leica SP5 or SP8 equipped with a 63X N.A. 1.4 PlanApo objective. Confocal stacks were acquired every 30s or 2 min before and after photobleaching on 13 z steps to compensate for movement in z during acquisition.

FRAP experiments were performed in pupae expressing ATP-α::GFP with Sqh::RFP^{crispr} to localize AJ level and RFP-nls used as a marker of *aka*^{L200} cells. ATP-α::GFP was bleached (488 nm laser at 60% power, 2 iterations of 1.293 s, 2.5µm*1.5µm) using a LSM Leica SP5 or SP8 equipped with a 63X N.A. 1.4 PlanApo objective. Confocal stacks were acquired every 30s or 2 min before and after photobleaching on 6 or 14 z steps to compensate for movement in z during acquisition.

Nanoablation

Laser ablation was performed on live pupae aged for 16h to 19h APF using a Leica SP5 confocal microscope equipped with a 63X N.A. 1.4 PlanApo objective. Ablation was carried out on epithelial cell membranes at SJ/AJ level with a two-photon laser-type Mai-Tai HP from Spectra Physics set to 800 nm and a laser power of 2.9W. LAS AF parameters are laser trans 50%, gain 70%, offset 35% and 1 iteration of 1.293 s.

QUANTITATION AND STATISTICAL ANALYSIS

Signal recovery upon photobleaching

In all FRAP experiments, ROI 1 corresponds to the photobleached area, ROI 2 to the area used as a control for general photobleaching of the sample across time and ROI 3 to the background. ROI 1 and ROI 3 had the same dimensions in all FRAP experiments (2µm*1.5µm for Aka::GFP ; 2.5µm*1.5µm for ATP-α::GFP).

For Aka::GFP, a sum slice of 8 z (4µm in total) was applied in order to collect the entire signal. ROI 2 was considered as the fluorescence of the entire field.

For ATP-α::GFP, a sum slice, of 2 z (1µm in total) of the plan just below AJ marked by Sqh::RFP^{crispr} and the one below, was applied to avoid z movements. ROI 2 was considered as the fluorescence of the entire field.

Then, we used EasyFRAP-web [54] for all data processing and to extract normalized values. The I(t) which correspond to the fluorescence intensity across time was calculated as described:

First, the fluorescence intensity is corrected by subtracting the background:

$$I(t)_{ROI1'} = I(t)_{ROI1} - I(t)_{ROI3}$$

$$I(t)_{ROI2'} = I(t)_{ROI2} - I(t)_{ROI3}$$

Then, values of fluorescence intensity are normalized in this way:

$$I(t)_{\text{double norm}} = \left(\frac{\frac{1}{n_{pre}} \times \sum_{t=1}^{n_{pre}} I(t)_{ROI2'}}{I(t)_{ROI2'}} \right) \times \left(\frac{I(t)_{ROI1'}}{\frac{1}{n_{pre}} \times \sum_{t=1}^{n_{pre}} I(t)_{ROI1'}} \right)$$

We decided to take value from full scale normalization in order to have a curve starting from 0:

$$I(t)_{\text{fullscale norm}} = \frac{I(t)_{\text{double norm}} - I(t_{\text{postbleach}})_{\text{double norm}}}{1 - I(t_{\text{postbleach}})_{\text{double norm}}}$$

Recovery curves were then fitted assuming a one-phase exponential association equation using the GraphPad Prism 8.0 software:

$$I(t)_{\text{fullscale norm}} = I(t)_{\text{max fullscale norm}} \times (1 - e^{-K \times t})$$

We admitted that $I(t)_{\max \text{fullscale norm}}$ is the maximum value based on the fitted curve for the post-bleach time (20 min for Aka::GFP and 18 min for ATP-α::GFP) and it is considered as the immobile fraction. $t_{1/2}$ was deduced when $I(t)_{\text{fullscale norm}} = 0{,}5 \times I(t)_{\max \text{fullscale norm}}$ which occurred at $t = \frac{-\ln(0{,}5)}{K}$.

Fluorescence vertex analysis

Sum slices were applied to different experiments. A segmented line of 10 pixels width was used to measure Aka signal in WT and *Gli* ^{dv3} /*M6* ^{W186} mutant vertex. Using the same width, lines were drawn to extract background fluorescence signal and the background signal was subtracted to each vertex quantification. After, data were standardized between 0 and 1 to allow visual representation with 1 corresponding to the highest signal of Aka at vertex in each experiment analyzed and 0 the lowest.

Line scan fluorescence analysis

Maximal projection were applied and a 20 pixels width line was drawn from apical part to basal part (Figure 3E-3H') or from vertex 1 to vertex 2, spanning the BCJ (Figures 3I', 4B', 4C', S4B', S4C', S4E' and S4F'). Then gray value was plotted across length of the line.

Statistical tests

All information concerning the statistical details are provided in the main text and in figure legends, including the number of samples analyzed for each experiment. Scattered plots use the following standards: thick line indicate the means and errors bars represent the standard deviations. Boxplots with connected line use the following standards: dots represent mean and the total colored areas show SD.

Statistical analyses were performed using the GraphPad Prism 8.0 software. The Shapiro-Wilk normality test was used to confirm the normality of the data and the F-test to verify the equality of SD. The statistical difference of Gaussian data sets was analyzed using the Student unpaired two-tailed t test. For contingency analysis (Figure S1E), a Fisher's exact test was used. Statistical significances were represented as follow: p value > 0.05 NS (not significant) and p value $\leq$ 0.0001 ****.

Legends for Supplemental Videos

Video S1- Tricellular Adherens Junction (tAJ) formation. Related to Figure 1.
Representative movie of tAJ formation using Sdk::GFP (green) and Sqh::RFP (magenta) in *Drosophila melanogaster* epithelial cell notum. Time is min::sec and t0 is the Metaphase to Anaphase transition.

Video S2- Finger like protrusions (FLP) formation during cytokinesis of wild type epithelial cell. Related to Figure 1 and Figure S1.
Representative movie of FLP formation using ATP-α::GFP (green), Sqh::RFP (magenta) and nls::RFP (magenta; representing wild type cells) in wild type *Drosophila melanogaster* epithelial cell notum. Time is min::sec and t0 is the Metaphase to Anaphase transition.

Video S3- Tricellular Septate Junction (tSJ) formation. Related to Figure 1.
Representative movie of tSJ formation using GFP::M6 (green) and Sqh::RFP (magenta) in *Drosophila melanogaster* epithelial cell notum. Time is min::sec and t0 is the Metaphase to Anaphase transition.

Video S4- Finger like protrusions (FLP) formation during cytokinesis of aka mutant epithelial cell. Related to Figure 1 and Figure S1.
Representative movie of FLP formation using ATP-α::GFP (green), Sqh::RFP (magenta) and nls::RFP (magenta; representing wild type cells) in *aka*^{L200} *Drosophila melanogaster* epithelial cell notum. Time is min::sec and t0 is the Metaphase to Anaphase transition.

References

1. Bosveld, F., Wang, Z., and Bellaiche, Y. (2018). Tricellular junctions: a hot corner of epithelial biology. Current opinion in cell biology *54*, 80-88.
2. Higashi, T., and Miller, A.L. (2017). Tricellular junctions: how to build junctions at the TRICkiest points of epithelial cells. Molecular biology of the cell *28*, 2023-2034.
3. Furuse, M., Izumi, Y., Oda, Y., Higashi, T., and Iwamoto, N. (2014). Molecular organization of tricellular tight junctions. Tissue Barriers *2*, e28960.
4. Finegan, T.M., Hervieux, N., Nestor-Bergmann, A., Fletcher, A.G., Blanchard, G.B., and Sanson, B. (2019). The tricellular vertex-specific adhesion molecule Sidekick facilitates polarised cell intercalation during Drosophila axis extension. PLoS biology *17*, e3000522.
5. Uechi, H., and Kuranaga, E. (2019). The Tricellular Junction Protein Sidekick Regulates Vertex Dynamics to Promote Bicellular Junction Extension. Developmental cell *50*, 327-338 e325.
6. Letizia, A., He, D., Astigarraga, S., Colombelli, J., Hatini, V., Llimargas, M., and Treisman, J.E. (2019). Sidekick Is a Key Component of Tricellular Adherens Junctions that Acts to Resolve Cell Rearrangements. Developmental cell *50*, 313-326 e315.
7. Schulte, J., Tepass, U., and Auld, V.J. (2003). Gliotactin, a novel marker of tricellular junctions, is necessary for septate junction development in Drosophila. The Journal of cell biology *161*, 991-1000.

8. Byri, S., Misra, T., Syed, Z.A., Batz, T., Shah, J., Boril, L., Glashauser, J., Aegerter-Wilmsen, T., Matzat, T., Moussian, B., et al. (2015). The Triple-Repeat Protein Anakonda Controls Epithelial Tricellular Junction Formation in Drosophila. Developmental cell *33*, 535-548.
9. Hildebrandt, A., Pflanz, R., Behr, M., Tarp, T., Riedel, D., and Schuh, R. (2015). Bark beetle controls epithelial morphogenesis by septate junction maturation in Drosophila. Developmental biology *400*, 237-247.
10. Zappia, M.P., Brocco, M.A., Billi, S.C., Frasch, A.C., and Ceriani, M.F. (2011). M6 membrane protein plays an essential role in Drosophila oogenesis. PloS one *6*, e19715.
11. Dunn, B.S., Rush, L., Lu, J.Y., and Xu, T. (2018). Mutations in the Drosophila tricellular junction protein M6 synergize with Ras(V12) to induce apical cell delamination and invasion. Proceedings of the National Academy of Sciences of the United States of America *115*, 8358-8363.
12. Fristrom, D.K. (1982). Septate junctions in imaginal disks of Drosophila: a model for the redistribution of septa during cell rearrangement. The Journal of cell biology *94*, 77-87.
13. Graf, F., Noirot-Timothee, C., and Noirot, C. (1982). The specialization of septate junctions in regions of tricellular junctions. I. Smooth septate junctions (=continuous junctions). J Ultrastruct Res *78*, 136-151.
14. Noirot-Timothee, C., Graf, F., and Noirot, C. (1982). The specialization of septate junctions in regions of tricellular junctions. II. Pleated septate junctions. J Ultrastruct Res *78*, 152-165.
15. Daniel, E., Daude, M., Kolotuev, I., Charish, K., Auld, V., and Le Borgne, R. (2018). Coordination of Septate Junctions Assembly and Completion of Cytokinesis in Proliferative Epithelial Tissues. Current biology : CB *28*, 1380-1391 e1384.
16. Bellen, H.J., Levis, R.W., He, Y., Carlson, J.W., Evans-Holm, M., Bae, E., Kim, J., Metaxakis, A., Savakis, C., Schulze, K.L., et al. (2011). The Drosophila gene disruption project: progress using transposons with distinctive site specificities. Genetics *188*, 731-743.
17. Buszczak, M., Paterno, S., Lighthouse, D., Bachman, J., Planck, J., Owen, S., Skora, A.D., Nystul, T.G., Ohlstein, B., Allen, A., et al. (2007). The carnegie protein trap library: a versatile tool for Drosophila developmental studies. Genetics *175*, 1505-1531.
18. Founounou, N., Loyer, N., and Le Borgne, R. (2013). Septins regulate the contractility of the actomyosin ring to enable adherens junction remodeling during cytokinesis of epithelial cells. Developmental cell *24*, 242-255.
19. Herszterg, S., Leibfried, A., Bosveld, F., Martin, C., and Bellaiche, Y. (2013). Interplay between the dividing cell and its neighbors regulates adherens junction formation during cytokinesis in epithelial tissue. Developmental cell *24*, 256-270.
20. Pinheiro, D., Hannezo, E., Herszterg, S., Bosveld, F., Gaugue, I., Balakireva, M., Wang, Z., Cristo, I., Rigaud, S.U., Markova, O., et al. (2017). Transmission of cytokinesis forces via E-cadherin dilution and actomyosin flows. Nature *545*, 103-107.
21. Guillot, C., and Lecuit, T. (2013). Adhesion disengagement uncouples intrinsic and extrinsic forces to drive cytokinesis in epithelial tissues. Developmental cell *24*, 227-241.
22. Wang, Z., Bosveld, F., and Bellaiche, Y. (2018). Tricellular junction proteins promote disentanglement of daughter and neighbour cells during epithelial cytokinesis. Journal of cell science *131*.
23. Astigarraga, S., Douthit, J., Tarnogorska, D., Creamer, M.S., Mano, O., Clark, D.A., Meinertzhagen, I.A., and Treisman, J.E. (2018). Drosophila Sidekick is required in developing photoreceptors to enable visual motion detection. Development *145*.
24. Lecuit, T., and Yap, A.S. (2015). E-cadherin junctions as active mechanical integrators in tissue dynamics. Nature cell biology *17*, 533-539.
25. Harris, T.J., and Tepass, U. (2010). Adherens junctions: from molecules to morphogenesis. Nature reviews. Molecular cell biology *11*, 502-514.
26. Ikenouchi, J., Furuse, M., Furuse, K., Sasaki, H., Tsukita, S., and Tsukita, S. (2005). Tricellulin constitutes a novel barrier at tricellular contacts of epithelial cells. The Journal of cell biology *171*, 939-945.

27. Masuda, S., Oda, Y., Sasaki, H., Ikenouchi, J., Higashi, T., Akashi, M., Nishi, E., and Furuse, M. (2011). LSR defines cell corners for tricellular tight junction formation in epithelial cells. Journal of cell science *124*, 548-555.
28. Higashi, T., Tokuda, S., Kitajiri, S., Masuda, S., Nakamura, H., Oda, Y., and Furuse, M. (2013). Analysis of the 'angulin' proteins LSR, ILDR1 and ILDR2--tricellulin recruitment, epithelial barrier function and implication in deafness pathogenesis. Journal of cell science *126*, 966-977.
29. Higashi, T., Arnold, T.R., Stephenson, R.E., Dinshaw, K.M., and Miller, A.L. (2016). Maintenance of the Epithelial Barrier and Remodeling of Cell-Cell Junctions during Cytokinesis. Current biology : CB *26*, 1829-1842.
30. Yan, Y., Narayanan, V., and Lagenaur, C. (1996). Expression of members of the proteolipid protein gene family in the developing murine central nervous system. The Journal of comparative neurology *370*, 465-478.
31. Lagenaur, C., Kunemund, V., Fischer, G., Fushiki, S., and Schachner, M. (1992). Monoclonal M6 antibody interferes with neurite extension of cultured neurons. Journal of neurobiology *23*, 71-88.
32. Gilula, N.B., Branton, D., and Satir, P. (1970). The septate junction: a structural basis for intercellular coupling. Proceedings of the National Academy of Sciences of the United States of America *67*, 213-220.
33. Sharifkhodaei, Z., Gilbert, M.M., and Auld, V.J. (2019). Scribble and Discs Large mediate tricellular junction formation. Development *146*.
34. Gilbert, M., Smith, J., Roskams, A.J., and Auld, V.J. (2001). Neuroligin 3 is a vertebrate gliotactin expressed in the olfactory ensheathing glia, a growth-promoting class of macroglia. Glia *34*, 151-164.
35. Zhang, C., Milunsky, J.M., Newton, S., Ko, J., Zhao, G., Maher, T.A., Tager-Flusberg, H., Bolliger, M.F., Carter, A.S., Boucard, A.A., et al. (2009). A neuroligin-4 missense mutation associated with autism impairs neuroligin-4 folding and endoplasmic reticulum export. The Journal of neuroscience : the official journal of the Society for Neuroscience *29*, 10843-10854.
36. Chanda, S., Hale, W.D., Zhang, B., Wernig, M., and Sudhof, T.C. (2017). Unique versus Redundant Functions of Neuroligin Genes in Shaping Excitatory and Inhibitory Synapse Properties. The Journal of neuroscience : the official journal of the Society for Neuroscience *37*, 6816-6836.
37. Zhang, B., Chen, L.Y., Liu, X., Maxeiner, S., Lee, S.J., Gokce, O., and Sudhof, T.C. (2015). Neuroligins Sculpt Cerebellar Purkinje-Cell Circuits by Differential Control of Distinct Classes of Synapses. Neuron *87*, 781-796.
38. Kim, J.A., Kim, D., Won, S.Y., Han, K.A., Park, D., Cho, E., Yun, N., An, H.J., Um, J.W., Kim, E., et al. (2017). Structural Insights into Modulation of Neurexin-Neuroligin Trans-synaptic Adhesion by MDGA1/Neuroligin-2 Complex. Neuron *94*, 1121-1131 e1126.
39. Gangwar, S.P., Zhong, X., Seshadrinathan, S., Chen, H., Machius, M., and Rudenko, G. (2017). Molecular Mechanism of MDGA1: Regulation of Neuroligin 2:Neurexin Trans-synaptic Bridges. Neuron *94*, 1132-1141 e1134.
40. Elegheert, J., Cvetkovska, V., Clayton, A.J., Heroven, C., Vennekens, K.M., Smukowski, S.N., Regan, M.C., Jia, W., Smith, A.C., Furukawa, H., et al. (2017). Structural Mechanism for Modulation of Synaptic Neuroligin-Neurexin Signaling by MDGA Proteins. Neuron *96*, 242-244.
41. Litwack, E.D., Babey, R., Buser, R., Gesemann, M., and O'Leary, D.D. (2004). Identification and characterization of two novel brain-derived immunoglobulin superfamily members with a unique structural organization. Molecular and cellular neurosciences *25*, 263-274.
42. Bieber, A.J., Snow, P.M., Hortsch, M., Patel, N.H., Jacobs, J.R., Traquina, Z.R., Schilling, J., and Goodman, C.S. (1989). Drosophila neuroglian: a member of the immunoglobulin superfamily with extensive homology to the vertebrate neural adhesion molecule L1. Cell *59*, 447-460.
43. Genova, J.L., and Fehon, R.G. (2003). Neuroglian, Gliotactin, and the Na+/K+ ATPase are essential for septate junction function in Drosophila. The Journal of cell biology *161*, 979-989.

44. Banerjee, S., Sousa, A.D., and Bhat, M.A. (2006). Organization and function of septate junctions: an evolutionary perspective. Cell Biochem Biophys *46*, 65-77.
45. Fox, R.M., and Andrew, D.J. (2015). Changes in organelle position and epithelial architecture associated with loss of CrebA. Biology open *4*, 317-330.
46. Babatz, F., Naffin, E., and Klambt, C. (2018). The Drosophila Blood-Brain Barrier Adapts to Cell Growth by Unfolding of Pre-existing Septate Junctions. Developmental cell *47*, 697-710 e693.
47. Schmid, E.M., Bakalar, M.H., Choudhuri, K., Weichsel, J., Ann, H., Geissler, P.L., Dustin, M.L., and Fletcher, D.A. (2016). Size-dependent protein segregation at membrane interfaces. Nat Phys *12*, 704-711.
48. Auld, V.J., Fetter, R.D., Broadie, K., and Goodman, C.S. (1995). Gliotactin, a novel transmembrane protein on peripheral glia, is required to form the blood-nerve barrier in Drosophila. Cell *81*, 757-767.
49. Stork, T., Thomas, S., Rodrigues, F., Silies, M., Naffin, E., Wenderdel, S., and Klambt, C. (2009). Drosophila Neurexin IV stabilizes neuron-glia interactions at the CNS midline by binding to Wrapper. Development *136*, 1251-1261.
50. Martin, A.C., Gelbart, M., Fernandez-Gonzalez, R., Kaschube, M., and Wieschaus, E.F. (2010). Integration of contractile forces during tissue invagination. The Journal of cell biology *188*, 735-749.
51. Claret, S., Jouette, J., Benoit, B., Legent, K., and Guichet, A. (2014). PI(4,5)P2 Produced by the PI4P5K SKTL Controls Apical Size by Tethering PAR-3 in Drosophila Epithelial Cells. Current biology : CB *24*, 1071-1079.
52. Calleja, M., Moreno, E., Pelaz, S., and Morata, G. (1996). Visualization of gene expression in living adult Drosophila. Science *274*, 252-255.
53. Schindelin, J., Arganda-Carreras, I., Frise, E., Kaynig, V., Longair, M., Pietzsch, T., Preibisch, S., Rueden, C., Saalfeld, S., Schmid, B., et al. (2012). Fiji: an open-source platform for biological-image analysis. Nature methods *9*, 676-682.
54. Koulouras, G., Panagopoulos, A., Rapsomaniki, M.A., Giakoumakis, N.N., Taraviras, S., and Lygerou, Z. (2018). EasyFRAP-web: a web-based tool for the analysis of fluorescence recovery after photobleaching data. Nucleic acids research *46*, W467-W472.
55. Gho, M., Lecourtois, M., Geraud, G., Posakony, J.W., and Schweisguth, F. (1996). Subcellular localization of Suppressor of Hairless in Drosophila sense organ cells during Notch signalling. Development *122*, 1673-1682.
56. Gho, M., Bellaiche, Y., and Schweisguth, F. (1999). Revisiting the Drosophila microchaete lineage: a novel intrinsically asymmetric cell division generates a glial cell. Development *126*, 3573-3584.

KEY RESOURCES TABLE

REAGENT or RESOURCE	SOURCE	IDENTIFIER
Antibodies		
Mouse anti-Cora (1:200)	DSHB	C615.16, RRID: AB_1161644
Rat anti-DE-cad (1:500)	DSHB	DCAD2
Mouse anti-Dlg (1:500)	DSHB	4F3
Mouse anti-GFP (1:200)	Roche	Clone 7.1
Rabbit anti-Aka (1:2000)	[8]	N/A
Mouse anti-Gli (1:200)	[48]	1F61D4
Guinea pig Anti-Sdk (1:200)	[23]	N/A
Rabbit anti-Nrx-IV (1:1000)	[49]	N/A
Cy2-, Cy3- and Cy5-coupled secondary antibodies (1:300)	The Jackson Laboratory	N/A
Alexa Fluor™ 647 Phalloidin (1:500)	Thermo Fisher Scientific	Cat#A22287
Chemicals, Peptides, and Recombinant Proteins		
Paraformaldehyde	EMS	19340-72
Triton X-100	Euromedex	2000B
Phosphate Buffered Saline	Lonza	BE17-515F
Voltalef	VWR	24627.188
Experimental Models: Organisms/Strains		
D.melanogaster: Sqh::GFP^{crispr}	InDroso	N/A
D.melanogaster: Sqh::RFP^{crispr}	[15]	N/A
D.melanogaster: Aka::GFP	[8]	N/A
D.melanogaster: Aka::GFP, *Gli^{dv3}*, FRT40A / CyO	This study	N/A
D.melanogaster: GFP::M6	[17]	CA 06602
D.melanogaster: Sdk::GFP	[17]	Bloomington 60169
D. melanogaster: ; ubi-RFP nls, FRT40A / (CyO) ; ATP-α::GFP, sqh-Sqh::mCherry / (TM6, *Tb^{1}*)	This study	N/A
D. melanogaster: sqh-GAP43::mCherry	[50]	N/A
D.melanogaster: hs-FLP ; *aka^{L200}*, FRT40A / CyO	This study	N/A
D.melanogaster: sdk$^{\Delta 15}$	[23]	N/A
D.melanogaster: Gli^{dv3}, FRT40A/CyO	[7]	N/A

D.melanogaster: w* ; UAS-Ras^{V12} ; *M6^{w186}*, FRT79E / TM6, *Tb^{1}*	[11]	N/A
D.melanogaster: hs-FLP ; If/CyO ; *M6^{w186}*, FRT79E / TM6, *Tb^{1}*	This study	N/A
D.melanogaster: yw, *ey*-FLP ; Act>y+Gal4, UAS-GFP ; *tub*-Gal80, FRT79E	[11]	N/A
D.melanogaster: yw, *hs*-FLP ; *ubi*-RFP nls, FRT40A / (CyO)	[51]	N/A
D.melanogaster: UAS-Cora-RNAi	VDRC	9788
D.melanogaster: UAS-Nrx-IV-RNAi	VDRC	108 128
D.melanogaster: pnr-Gal4 / TM6, *Tb^{1}*	[52]	N/A
Software and Algorithms		
Fiji	[53]	https://imagej.net/Fiji
Illustrator	Adobe Systems	Adobe Illustrator CS6
Prism 8	GraphPad	GraphPad
EasyFRAP-web	[54]	https://easyfrap.vmnet.upatras.gr/
Others		
Confocal Microscope	Leica	LSM TCS SPE, TCS SP5 and TCS SP8

Fig1

Click here to access/download;Figure;Esmangart de Bournonville_Fig1.jpg

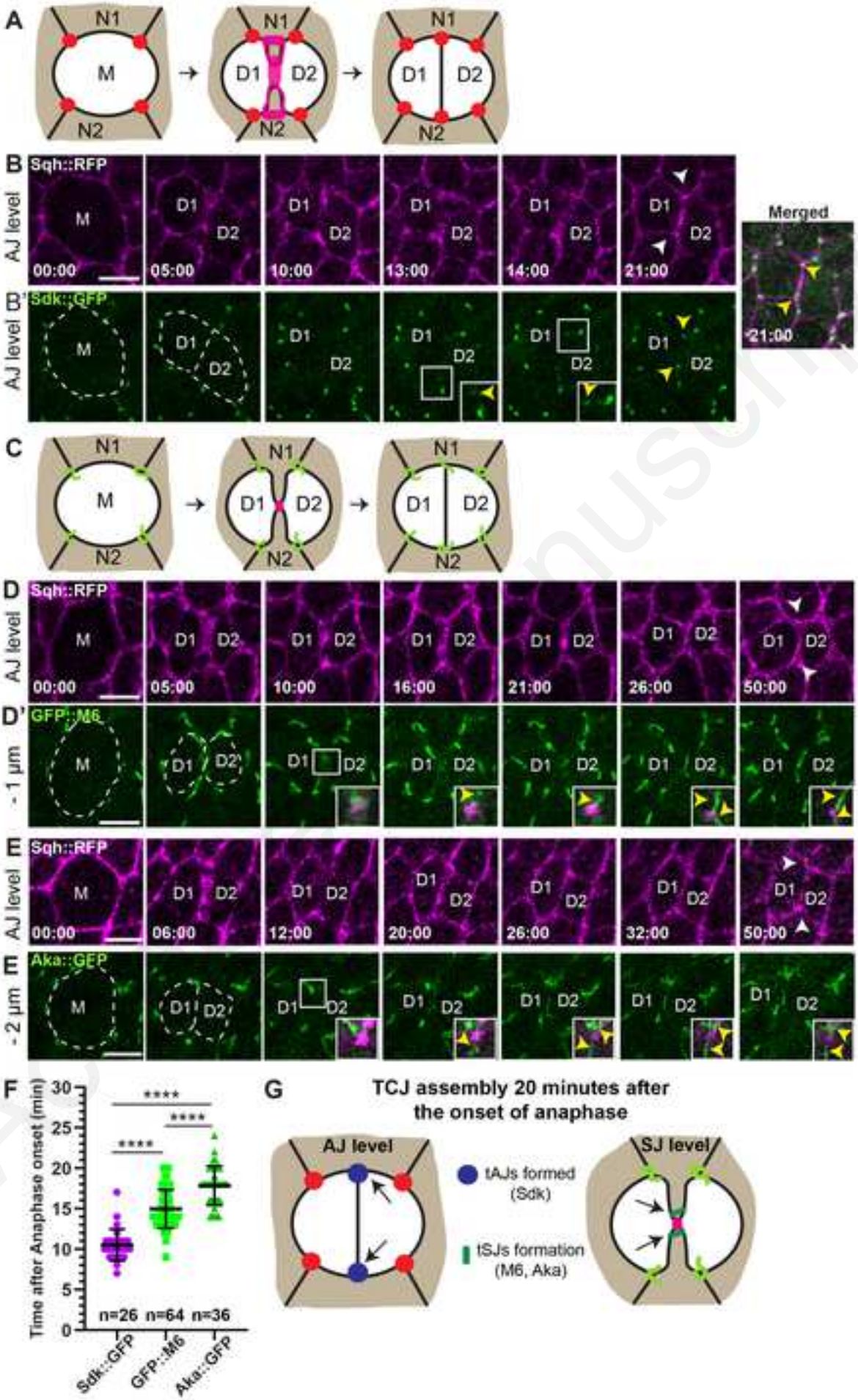

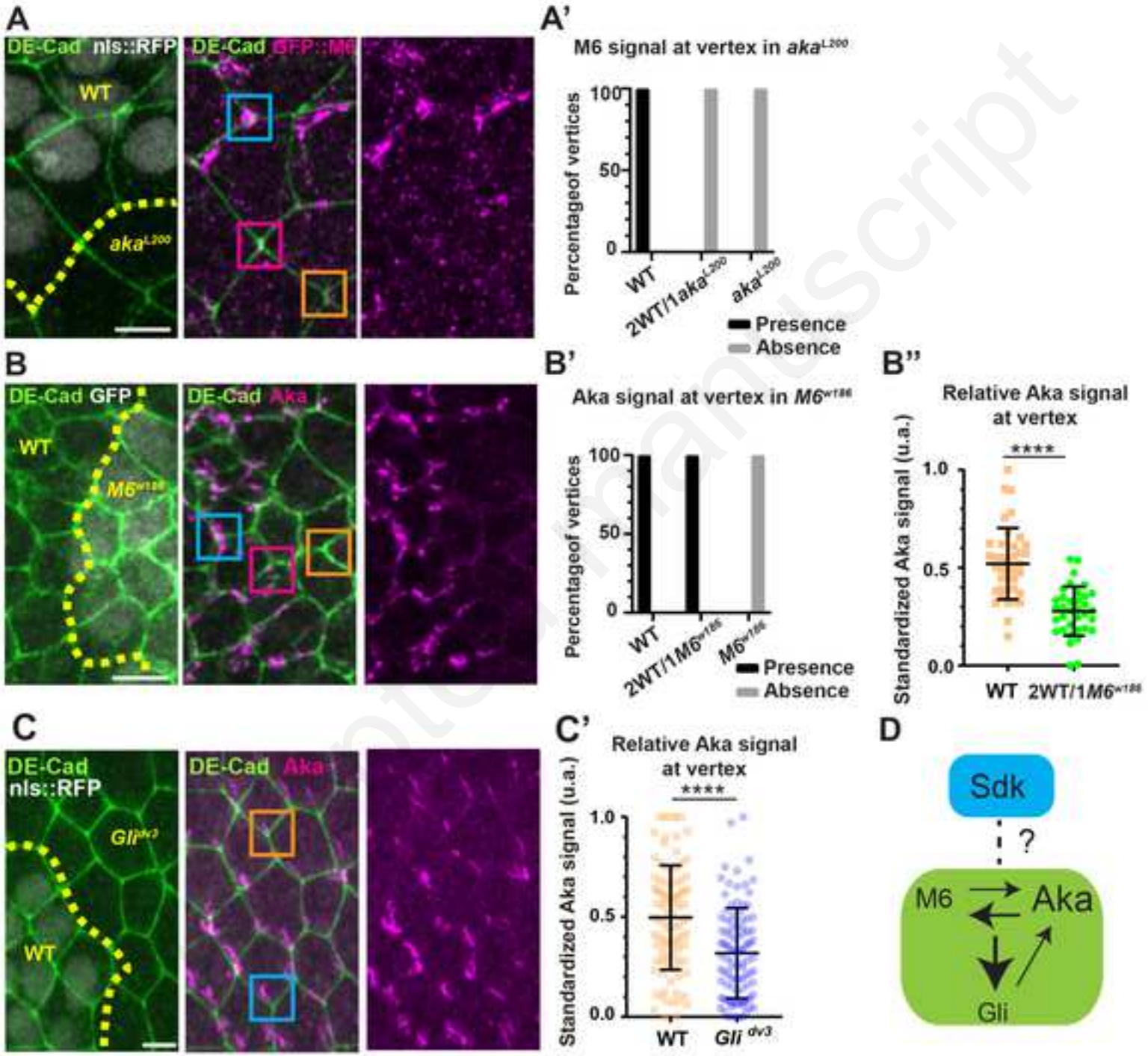

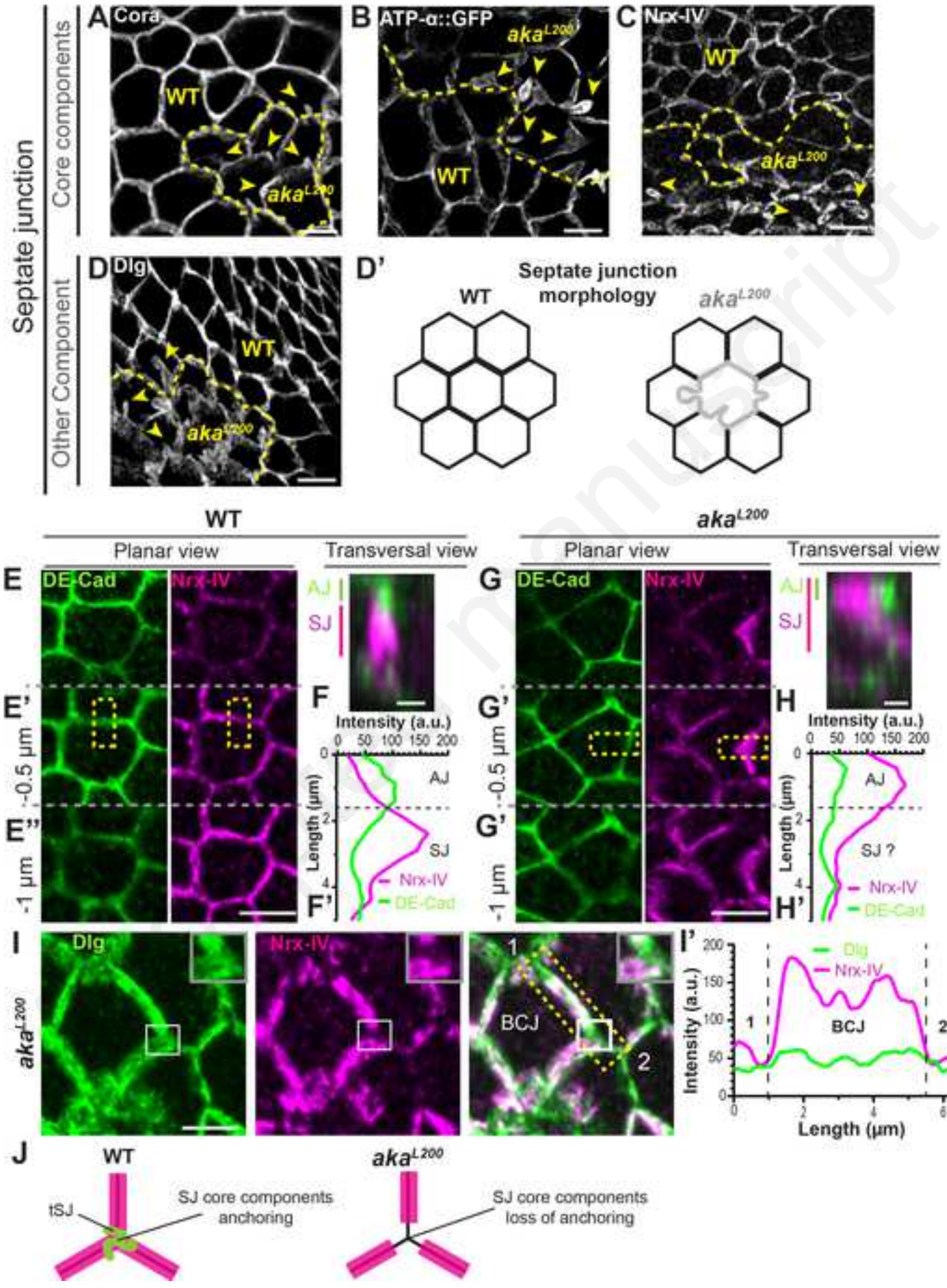

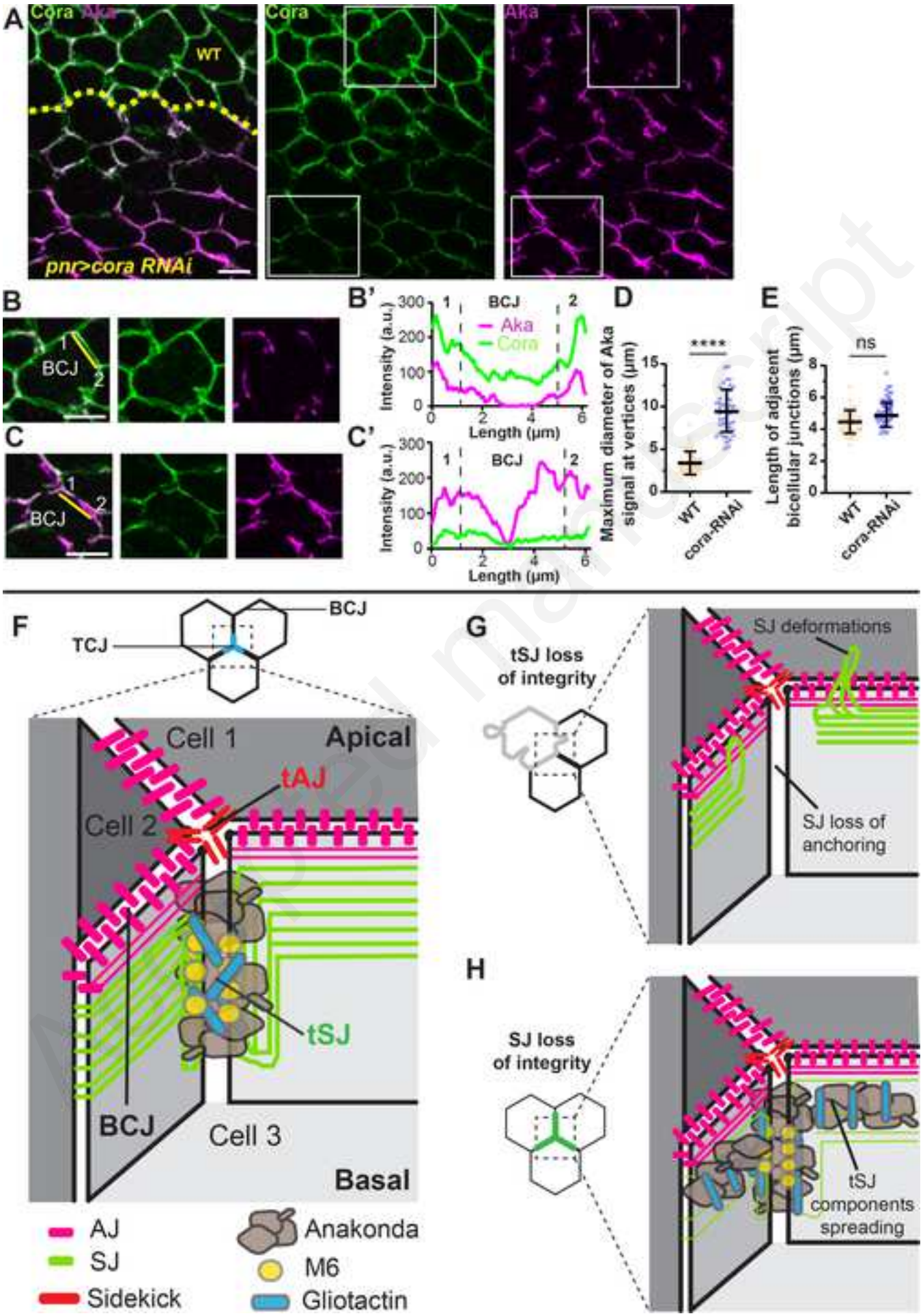

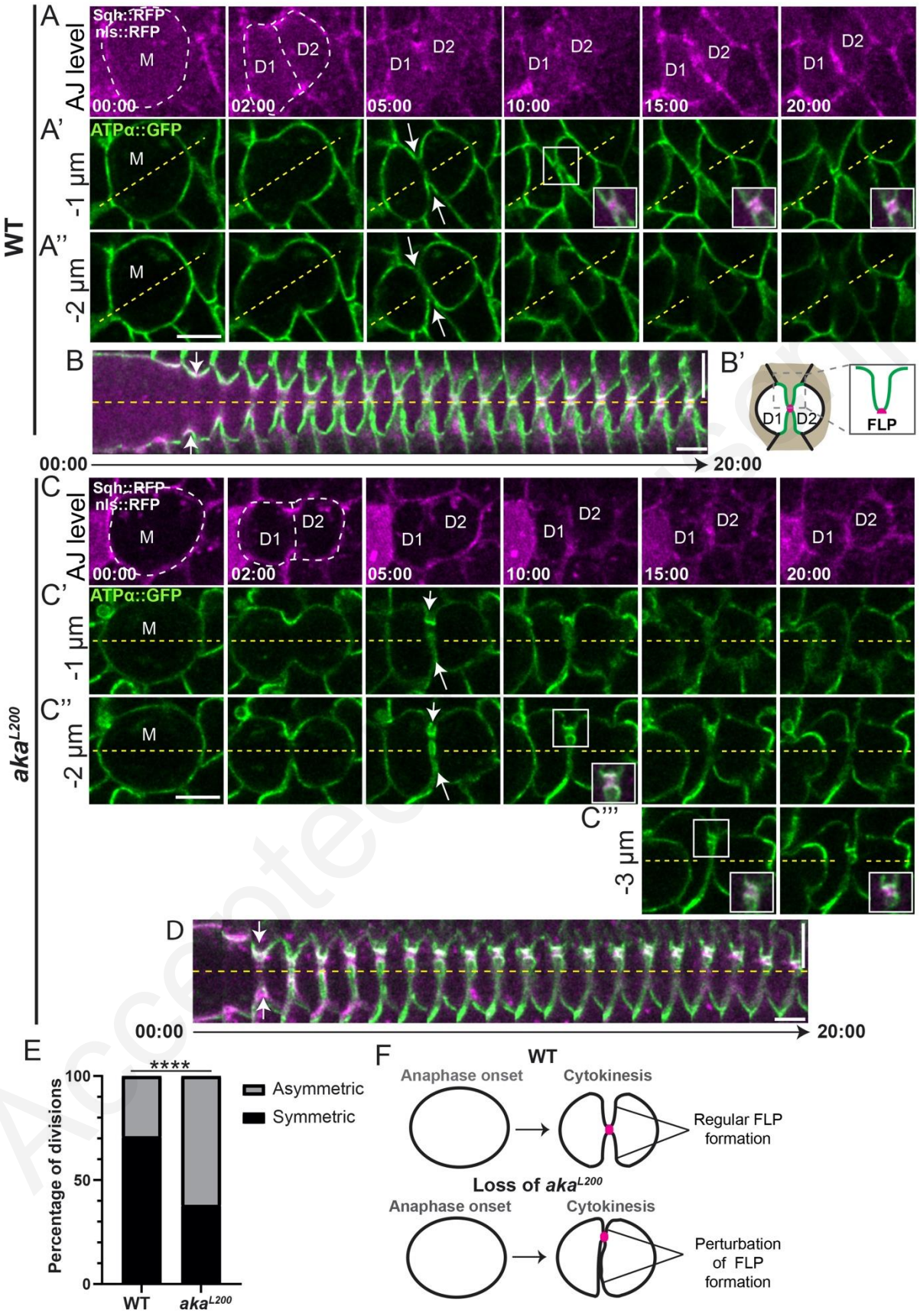

Figure S1: tSJ integrity is required to ensure FLP formation during cytokinesis. Related to Figure 1.

(A-D) Time-lapse imaging of FLP using Sqh::RFP^{crispr} (magenta, AJ) and ATPα::GFP (green, SJ) in wild type (marked by nls::RFP; A-B) and *aka*^{L200} (loss of nls::RFP; C-D) dividing cells, from plane view (A-A'' and C-C''') and with a kymograph representation (B and D). The mother cell is represented by the M and the daughters by D1 and D2. The white dashed lines highlight the divided cell and daughters. White arrows indicate FLP formation at SJ level. Yellow dashed lines define symmetry axis of the cell. White squares show high magnification of midbody (magenta) linking FLP. (B') Graphical representation of a FLP linking the two dividing cells and the adjacent neighbor cell. (E) Histogram representing the number of symmetric (black) and asymmetric (grey) FLP formation during cytokinesis in wild type (n = 14 divisions, 3 pupae) and *aka*^{L200} cells (n = 21 divisions, > 5 pupae). **** $p < 0.0001$, Fisher's exact test. (F) Schematic representation of the FLP formation upon cytokinesis. Loss of tSJ integrity leads to abnormal FLP shape and asymmetrical midbody formation at the new cell-cell interface. The horizontal scale bars represent 5µm (A and C), the vertical scale bars represent 5µm (B and D) and the horizontal scale bars represent 1min (B and D).

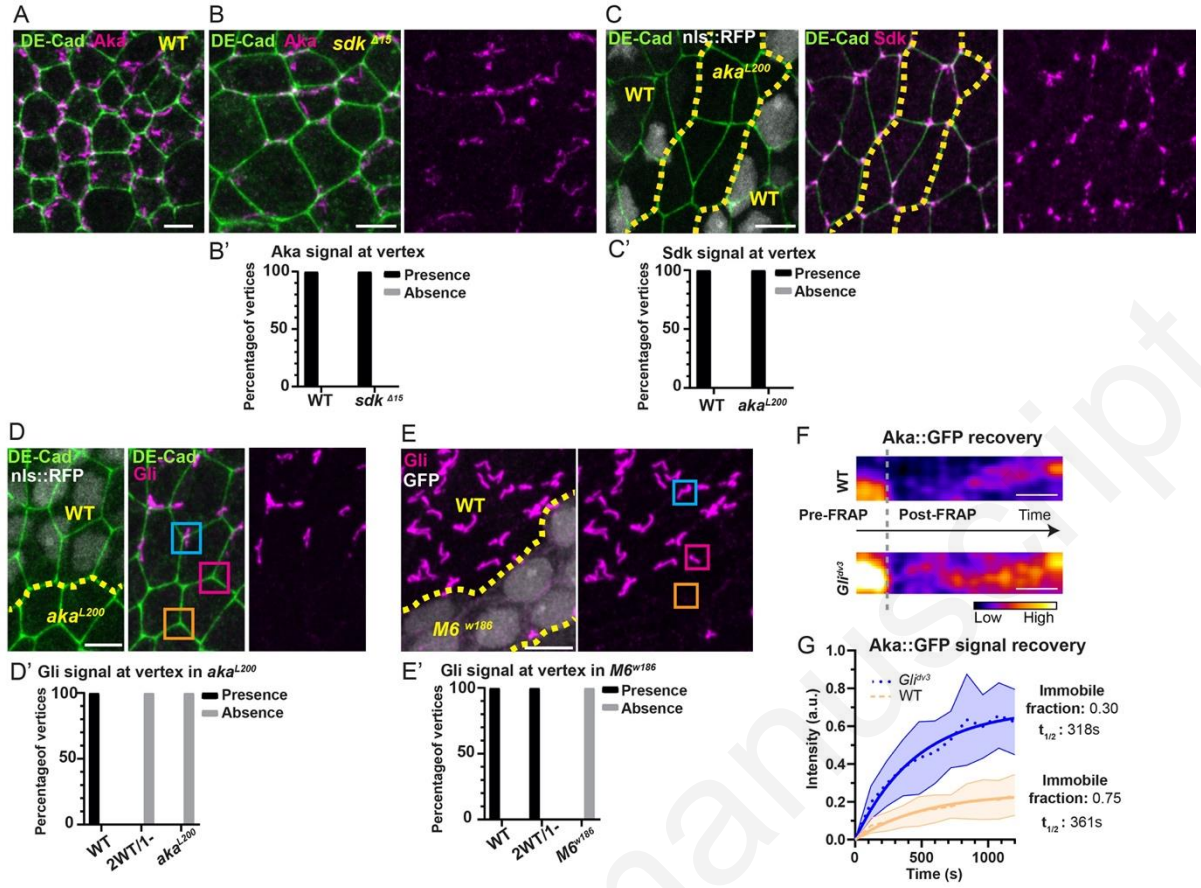

Figure S2: Aka, M6 and Gli are required for tSJs and dispensable for tAJs integrity. Related to Figure 2.

(A-B) Localization of Aka (anti-Aka, magenta) in wild type and *sdk*$^{\Delta 15}$ pupa. (B') Histogram representing the percentage of presence (black) or absence (gray) of Aka accumulation at the vertex in wild type (presence n = 100%, absence n = 0%) and *sdk*$^{\Delta 15}$ (presence n = 100, absence n = 0) (n = 100 vertices, 3 pupae). (C-E) show nota between 16h-18h APF stained for DE-cad (C and D ; anti-DE-cad, green) after heat-shock to induce clone of wild type (C and D nls::RFP positive; E, GFP negative) and mutant cells (C and D, nls::RFP negative; E, GFP positive) for tSJ components. (C) Localization of Sdk (anti-Sdk, magenta). The dashed yellow line separates wild type and *aka*^{L200} cells. (C') Histogram representing the percentage of presence (black) or absence (gray) of Sdk accumulation at the vertex in wild type (n presence n = 100%, absence n = 0%) and *aka*^{L200} (presence n = 100%, absence n = 0%) (n = 100 vertices, > 5 pupae). (D-E') Localization of Gli (anti-Gli, magenta). The dashed yellow line separates wild type and *aka*^{L200} (mutant) cells (D) or wild type and *M6*^{w186} (mutant) cells (E). Gli is enriched at the TCJ at wild-type vertex (blue square) and is no longer detected at a vertex of three *aka* mutant cells (D; orange square) or *M6* (E; orange

square) but also when Aka is lost in only one of the three cells participating in the vertex (D; pink square) but not for M6 (E; pink square). (D' and E') Histograms representing the percentage of presence (black) or absence (gray) of Gli accumulation at the vertex between 3 wild type cells (D' and E'; presence n = 100%, absence n = 0%), 2 wild type and 1 *aka*^{L200} cell (D'; presence n = 0%, absence n = 100%) or 1 *M6*^{w186} cell (E'; presence n = 100%, absence n = 0%) or 3 *aka*^{L200} cells (D'; presence n = 0%, absence n = 100%) or 3 *M6* ^{w186} cells (E'; presence n = 0%, absence n = 100%) (n = 100 vertices, > 5 pupae for each experiment). (F) Kymograph of the bleached region for Aka::GFP in wild type and *Gli*^{dv3} cells. A calibration bar shows LUT for gray value range. Scale bars show 5min. (G) Plot of Aka::GFP fluorescence recovery as a function of time for the conditions described in (F). Wild type: n = 11 FRAP experiments, 4 pupae; *Gli*^{dv3}: n = 12 FRAP experiments, 5 pupae. Data are mean ± SD. Solid line shows a simple exponential fit.

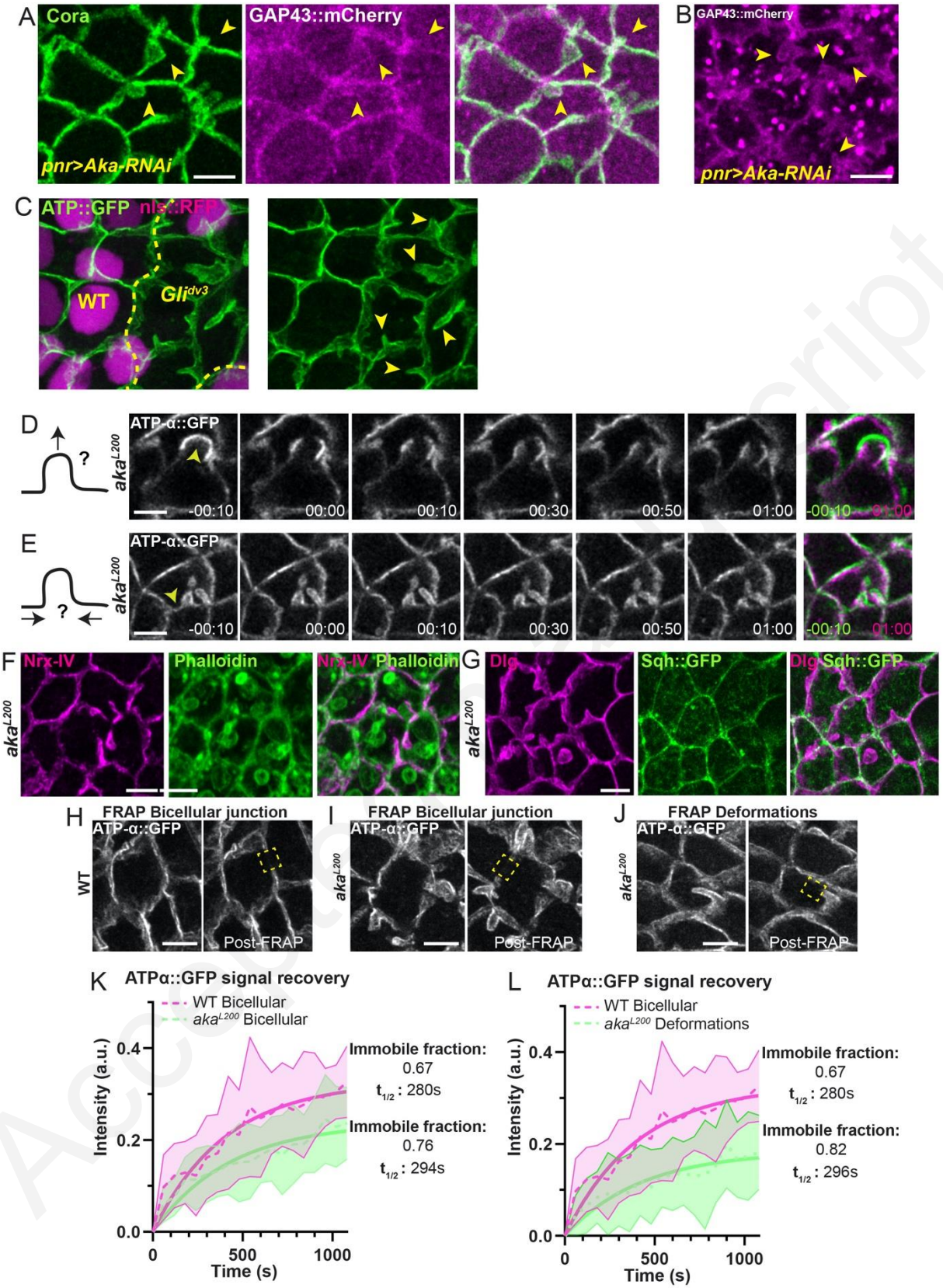

Figure S3: SJ deformations stabilization does not rely on mechanicals forces and SJ proteins exhibits increased stability within SJ deformations. Related to Figure 3.

(A-C) SJ and membrane morphology analysis using core components Cora (anti-Cora; A), GAP43::mCherry (A-B), or ATP-α::GFP (C) in wild type and upon knockdown of *aka* by RNAi approach (A-B) or in Gli^{dv3} cells (C). (A, B) GAP43::mCherry tagged membrane after fixation or in living samples (B) in *aka* RNAi area. (C) Localization of ATP-α::GFP in Gli^{dv3} cells. Yellow arrowheads indicate micrometric size SJ/membrane deformations. (D and E) Bi-photonic laser-based nanoablation of SJ deformations in aka^{L200} cells expressing ATP-α::GFP (white). Green and magenta pictures represent SJ deformations 10s before and 1min after ablation respectively. Yellow arrowheads show the ablation area. (F and G) Notum between 16h and 18h APF stained for Nrx-IV (anti-Nrx-IV, magenta; F), Dlg (anti-Dlg, magenta; G), Phalloidin (green; F) or expressing Sqh::GFP (green; G) in aka^{L200} cells. (H-J) Example of FRAP experiment of ATP-α::GFP at wild-type bicellular junction, aka^{L200} bicellular junction or SJ deformations in aka^{L200} cells. Yellow dashed rectangles show FRAP area. (K and L) Plot of ATP-α::GFP fluorescence recovery as a function of time for the conditions described in (H-J). Wild type bicellular junction: n= 8 FRAP experiments, 4 pupae; aka^{L200} bicellular junction: n= 6 FRAP experiments, 4 pupae. aka^{L200} SJ deformations: n= 9 FRAP experiments, 4 pupae. Data are mean ± SD. Solid line shows a simple exponential fit. The scale bars represent 5µm.

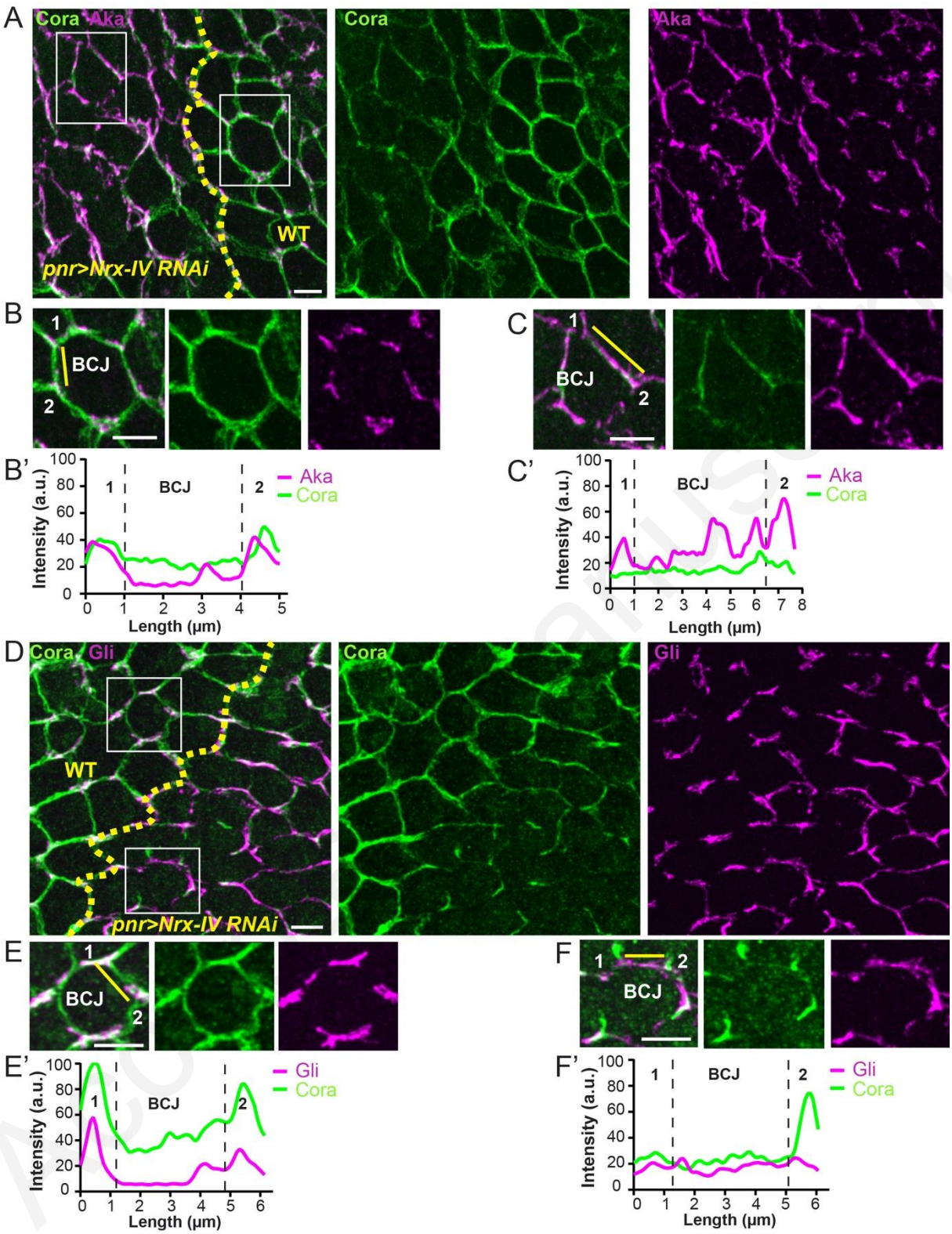

Figure S4: The presence of SJ core component is required to restrict Aka and Gli localization at vertex. Related to Figure 4.

(A-C, D-F) Localization of Aka (anti-Aka, magenta; A-C) or Gli (anti-Gli, magenta; D-F) in cells marked by Cora (anti-Cora, green) in wild type and cells expressing UAS::Nrx-IV RNAi under *pnr*-Gal4 control. The dashed yellow line separates wild type and Nrx-

IV-RNAi cells. Aka and Gli spread at the BCJ upon knockdown of Nrx-IV. White squares (A and D) show magnification (B-C and E-F) of wild type and knockdown cells for Nrx-IV. White dashed rectangles show the line scan used to obtain (B'-C' and E'-F') between two vertices represented by number 1 and 2. (B'-C' and E'-F') Plots representing Cora (green line) and Aka/Gli (magenta line) signals as a function of the length of cell-cell boundary in wild type and Nrx-IV-RNAi cells respectively. The scale bars represent 5μm.